APPLIED MATHEMATICS AND MECHANICS (ENGLISH EDITION)

Thermal vibration of functionally graded porous nanocomposite beams reinforced by graphene platelets*

M. H. YAS†, S. RAHIMI

Department of Mechanical Engineering, Razi University, Kermanshah 67346-67149, Iran

Abstract   The thermal vibration of functionally graded (FG) porous nanocomposite beams reinforced by graphene platelets (GPLs) is studied. The beams are exposed to the thermal gradient with a multilayer structure. The temperature varies linearly across the thickness direction. Three different types of dispersion patterns of GPLs as well as porosity distributions are presented. The material properties vary along the thickness direction. By using the mechanical parameters of closed-cell cellular solid, the variation of Poisson's ratio and the relation between the porosity coefficient and the mass density under the Gaussian random field (GRF) model are obtained. By using the Halpin-Tsai micromechanics model, the elastic modulus of the nanocomposite is achieved. The equations of motion based on the Timoshenko beam theory are obtained by using Hamilton's principle. These equations are discretized and solved by using the generalized differential quadrature method (GDQM) to obtain the fundamental frequencies. The effects of the weight fraction, the dispersion model, the geometry, and the size of GPLs, as well as the porosity distribution, the porosity coefficient, the boundary condition, the metal matrix, the slenderness ratio, and the thermal gradient are presented.

Key words   thermal vibration, functionally graded (FG), porous material, graphene platelet (GPL), Timoshenko beam

Chinese Library Classification   O327, O302
2010 Mathematics Subject Classification   74H45, 74S99, 74M25

1   Introduction

A porous medium refers to any material consisting of a substrate having a set of pores and multifunctional properties which could be promoted by introducing fillers. Metal foams have been known as a rather new type of materials. They have good features for applications such as low weight structure, energy absorption, and thermal handling[1–3]. The first attempt to apply porous metals for engineering applications dates back to the beginning of the 20th century.

Some researchers have studied the mechanical behavior of porous materials in recent years. Magnucki and Stasiewicz[4] studied a porous beam under elastic buckling load. They considered an isotropic porous beam with properties varying across the beam thickness, and studied the effects of porosity on the strength and buckling load of the beam analytically and numerically.

Grygorowicz et al.[5] investigated a sandwich beam with a metal foam core under buckling load. The mechanical parameters varied across the thickness direction, and two deformation hypotheses of the smooth cross-section including the classical broken line hypothesis and the non-linear hypothesis were considered. Chen et al.[6] investigated a functionally graded (FG) porous beam under buckling and bending loads. They used two different porosity distributions, derived the governing equations with the Timoshenko beam theory, and studied the effects of the porosity coefficient and the slenderness ratio on the critical buckling load, the maximum deflection, and the stress distribution.

Given the importance of vibrations in different practical and industrial applications and the development of porous material usage, the vibrations of porous materials have drawn increasing interest from researchers. Chen et al.[7] analyzed the FG porous beams made of open-cell metal foams. Ebrahimi et al.[8] inspected the thermal vibration of a temperature-dependent FG porous beam subjected to the uniform, linear, and non-linear thermal fields based on the Euler-Bernoulli beam theory, and studied the effects of the thermal effect, the porosity volume fraction, the material distribution profile, and the mode shape on the fundamental frequency of the beam.

Nanofillers added to porous materials must simultaneously have three features, viz., they should be ultra-lightweight so that the reinforced materials could remain in the light-weight structure category with their addition, they should be conducive to improve the mechanical properties of the reinforced materials, and they should have stable structure in the chemical viewpoint. Carbon nanotubes (CNTs)[9] and graphene platelets (GPLs)[10–11] have exceptionally the above-mentioned three features, and are appropriate candidates for nanofillers.

Numerous studies have been carried out to reveal the behaviors of nanocomposite structures strengthened by CNTs. Wu et al.[12] presented the non-linear vibration behavior of FG-CNT beams with initial geometric imperfections, and used the first-order shear deformation theory and the von Kármán geometric nonlinearity to derive the governing equations. Wattanasakulpong and Ungbhakorn[13] studied CNT beams under bending, buckling, and vibration, and used several shear deformation theories to derive the analytical solution. Mohammadi and Yas[14] used a three phase scale to model the elastic behavior of CNT strengthened polymers by considering the interfacial debonding. Yas et al.[15] studied the thermo-mechanical properties of multi-walled CNT/epoxy, functionalized the multi-walled CNTs by using the combination of H_2SO_4/HNO_3, and carried out several tests to obtain the temperature-dependent mechanical and thermal properties. Yas and Samadi[16] investigated the behavior of nanocomposite beams reinforced by single-walled CNTs under buckling and free vibration. Lai and Dangi[17] used the nonlocal theory of elasticity to present the thermal vibration of a temperature-dependent FG nonuniform Timoshenko nanobeam. Arefi et al.[18] studied the free vibration of FG polymer composite nanoplates reinforced by graphene nanoplatelets. Shahrjerdi and Yavar[19] studied the effects of temperature-dependent properties on the free vibrations of FG grapheme reinforced nanocomposite beams, and concluded that the natural frequency of temperature dependent materials was less than that of temperature independent materials. Song et al.[20] presented a dynamic analysis of FG polymer composite plates reinforced by graphene nanoplatelets.

In Refs. [10], [21], and [22], the performance of GPLs and CNTs in the modification of the mechanical parameters of structures was studied. It was deduced that the performance of GPLs was better. Among the good properties of graphene and its associated two-dimensional materials, the high thermal conductivity[23] shows high capacity to address the thermal handling challenge in electrical devices. Graphene holds high capacity in metal matrix composites for thermal handling because of its excellent thermal properties. However, the graphene/metal composites having both great thermal conductivity and low coefficient of thermal expansion have not yet been fully figured out. Currently, critical CNT-reinforced issues, including processing techniques, nanotube dispersion, interface, strengthening mechanisms, and mechanical properties, have been reviewed with an objective to achieve the homogeneous distribution of CNTs in

the matrix[24]. Since porous metals can be made into materials and used widely because of low weight, heat resistance, and non-combustibility, research on porous metals reinforced by GPLs in thermal environments can be interesting and useful. Although a lot of research has been done on the mechanical behaviors of nanocomposites reinforced by graphene and its derivatives, this set of research is still in the early stage. The main contribution of this research is to study the thermal vibration responses of porous like structures reinforced by GPLs. For this purpose, we consider three different porosity distributions as well as three different GPL dispersion models across the thickness direction. The theoretical formulation is derived according to the Timoshenko beam theory. The frequency is calculated by using the generalized differential quadrature method (GDQM). The effects of the GPL models and the porosity distributions on the beam vibration are highlighted. To accomplish the most effective beam stiffness, the best porosity distribution and the best GPL model are investigated. Finally, the effect of the thermal gradient is studied.

2 Porosity distributions, GPL models, and mechanical properties

A multilayer beam with the thickness h, the width b, and the length L in the (x, y, z) coordinate system is considered, as shown in Fig. 1. The x-axis is on the mid-plane, and the z-axis is across the thickness direction.
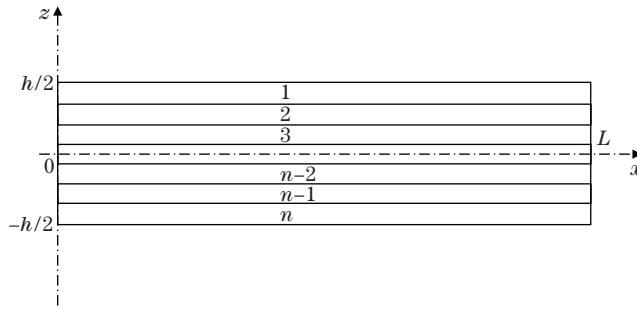

Fig. 1   Configuration of the studied beam

Figure 2 shows three different GPL distribution models, i.e., A, B, and C, for the non-uniform porosity distribution 1 (Distribution 1), the non-uniform porosity distribution 2 (Distribution 2), and the uniform porosity distribution 3 (Distribution 3). The GPL volume content V_{GPL} changes along the z-axis smoothly, and the maximum value of V_{GPL} is determined according to the specific porosity distribution. It is supposed that the total amounts of GPLs in three different GPL dispersion models are the same, which leads to $S_{i1} \neq S_{2i} \neq S_{3i}$.

It should be noticed that E_1' and E_2' are the maximum and the minimum Young's moduli of the non-uniform porous beams without GPLs, respectively, and E' is Young's modulus of the beam with a uniform porosity distribution. As shown in Fig. 2, the following relations are used to determine the mechanical properties of the FG porous nanocomposite beams with three different porosity distributions:

$$\rho(z) = \rho_1(1 - e_{\mathrm{m}}\lambda(z)), \quad E(z) = E_1(1 - e_0\lambda(z)), \quad G(z) = \frac{E(z)}{2(1 + \nu(z))}. \tag{1}$$

According to Ref. [25],

$$\alpha(z) = \alpha_1, \tag{2}$$

(a) Distribution 1 with three GPL dispersion patterns

(b) Distribution 2 with three GPL dispersion patterns

(c) Distribution 3 with three GPL dispersion patterns
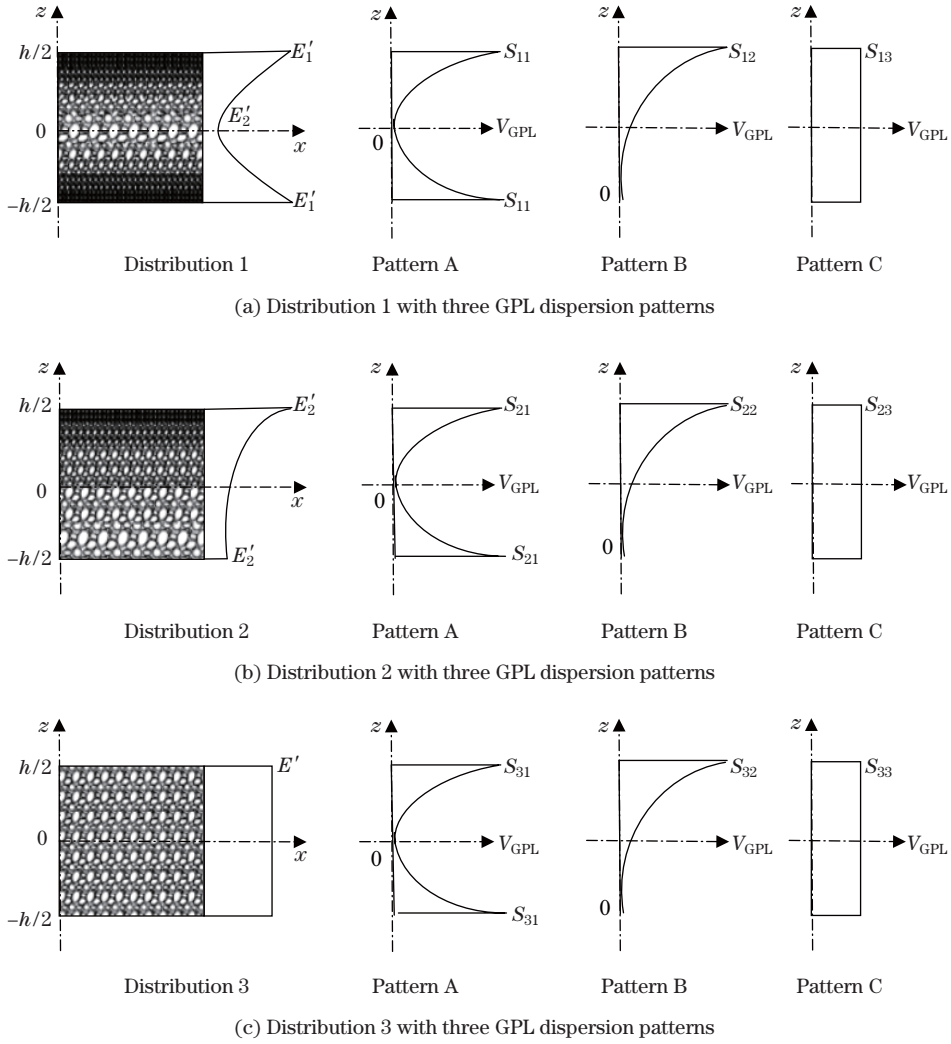
Fig. 2 Porosity distributions and GPL dispersion models

where

$$
\lambda(z) = \begin{cases} \cos(\pi z/h) & \text{for Distribution 1,} \\ \cos(\pi z/(2h) + \pi/4) & \text{for Distribution 2,} \\ \lambda & \text{for Distribution 3.} \end{cases} \tag{3}
$$

In the above equations, E_1, ρ_1, and α_1 are the maximum values of Young's modulus, the mass density, and the thermal expansion coefficient of the porous beam, respectively. The porosity coefficient is defined by

$$
e_0 = 1 - \frac{E_2'}{E_1'}. \tag{4}
$$

According to Ref. [26], in the Gaussian random field (GRF) model, the mechanical property of closed-cell cellular solid is expressed as

$$\frac{E(z)}{E_1} = \left(\frac{\rho(z)/\rho_1 + 0.121}{1.121}\right)^{2.3}, \quad 0.15 < \frac{\rho(z)}{\rho_1} < 1. \tag{5}$$

Using Eq. (5), the mass density coefficient e_m is determined by

$$e_\mathrm{m} = \frac{1.121(1 - \sqrt[2.3]{1 - e_0\lambda(z)})}{\lambda(z)}. \tag{6}$$

Also, Poisson's ratio $\nu(z)$ can be obtained based on the closed-cell GRF model[27] as

$$\nu(z) = 0.221p' + \nu_1(0.342p'^2 - 1.21p' + 1), \tag{7}$$

where ν_1 refers to Poisson's ratio of the non-porous matrix, and

$$p' = 1 - \frac{\rho(z)}{\rho_1} = 1.121(1 - \sqrt[2.3]{1 - e_0\lambda(z)}). \tag{8}$$

Assume that the beam total mass is the same under different porosity distributions. Then, the related term λ in Eq. (3) can be derived as

$$\lambda = \frac{1}{e_0} - \frac{1}{e_0}\left(\frac{M/h + 0.121}{1.121}\right)^{2.3}, \tag{9}$$

where M is identical for all porosity distributions, and is obtained by

$$M = \int_{-h/2}^{h/2} (1 - p')\mathrm{d}z. \tag{10}$$

In accord with the porosity distributions in Fig. 2, the volume fraction of GPLs can be shown as follows:

$$V_\mathrm{GPL} = \begin{cases} S_{i1}\left(1 - \cos\dfrac{\pi z}{h}\right) & \text{for Pattern A,} \\[2mm] S_{i2}\left(1 - \cos\left(\dfrac{\pi z}{h} + \dfrac{\pi}{4}\right)\right) & \text{for Pattern B,} \\[2mm] S_{i3} & \text{for Pattern C,} \end{cases} \tag{11}$$

where $i = 1, 2, 3$.

The weight fraction of GPLs W_GPL is related to V_GPL via

$$\frac{W_\mathrm{GPL}}{W_\mathrm{GPL} + \frac{\rho_\mathrm{GPL}}{\rho_\mathrm{M}} - \frac{\rho_\mathrm{GPL}}{\rho_\mathrm{M}}W_\mathrm{GPL}} \times \int_{-h/2}^{h/2} (1 - e_\mathrm{m}\lambda(z))\mathrm{d}z = \int_{-h/2}^{h/2} V_\mathrm{GPL}1 - e_\mathrm{m}\lambda(z)\mathrm{d}z. \tag{12}$$

In order to determine the elastic modulus of the non-porous nanocomposites, the Halpin-Tsai micromechanics model[10,28–30] is applied.

$$E_1 = \frac{3}{8}\left(\frac{1 + \xi_L^\mathrm{GPL}\eta_L^\mathrm{GPL}V_\mathrm{GPL}}{1 - \eta_L^\mathrm{GPL}V_\mathrm{GPL}}\right)E_\mathrm{M} + \frac{5}{8}\left(\frac{1 + \xi_W^\mathrm{GPL}\eta_W^\mathrm{GPL}V_\mathrm{GPL}}{1 - \eta_W^\mathrm{GPL}V_\mathrm{GPL}}\right)E_\mathrm{M}, \tag{13}$$

where

$$\begin{cases} \xi_L^\mathrm{GPL} = \dfrac{2l_\mathrm{GPL}}{t_\mathrm{GPL}}, \quad \xi_W^\mathrm{GPL} = \dfrac{2w_\mathrm{GPL}}{t_\mathrm{GPL}}, \\[3mm] \eta_L^\mathrm{GPL} = \dfrac{E_\mathrm{GPL}/E_\mathrm{M} - 1}{E_\mathrm{GPL}/E_\mathrm{M} + \xi_L^\mathrm{GPL}}, \quad \eta_W^\mathrm{GPL} = \dfrac{E_\mathrm{GPL}/E_\mathrm{M} - 1}{E_\mathrm{GPL}/E_\mathrm{M} + \xi_W^\mathrm{GPL}}. \end{cases} \tag{14}$$

In the above equations, w_{GPL}, l_{GPL}, and t_{GPL} denote the average width, the average length, and the average thickness of GPLs, respectively, and E_{M} is Young's modulus of the metal. The mass density ρ_1, the Poisson's ratio ν_1, and the thermal expansion coefficient α_1 of the metal matrix reinforced by GPLs are calculated by

$$\rho_1 = \rho_{\mathrm{GPL}}V_{\mathrm{GPL}} + \rho_{\mathrm{M}}V_{\mathrm{M}}, \quad \nu_1 = \nu_{\mathrm{GPL}}V_{\mathrm{GPL}} + \nu_{\mathrm{M}}V_{\mathrm{M}}, \quad \alpha_1 = \alpha_{\mathrm{GPL}}V_{\mathrm{GPL}} + \alpha_{\mathrm{M}}V_{\mathrm{GPL}}, \quad (15)$$

in which ρ_{GPL}, ν_{GPL}, α_{GPL}, and V_{GPL} are the mass density, the Poisson's ratio, the thermal expansion coefficient, and the volume fraction of GPLs, respectively, and ρ_{M}, ν_{M}, α_{M}, and $V_{\mathrm{M}} = 1 - V_{\mathrm{GPL}}$ are the mass density, the Poisson's ratio, the thermal expansion coefficient, and the volume fraction of the metal, respectively.

3 Theory and formulation

3.1 Equations of motion

Using the Timoshenko beam theory, the formulas of the deflection field of the beam are expressed in the x- and z-directions as follows:

$$U(x, z, t) = u_0(x, t) + z\phi(x, t), \quad W(x, z, t) = w_0(x, t), \quad (16)$$

where $u_0(x, t)$ and $w_0(x, t)$ stand for the axial and transverse displacement components on the mid-plane ($z = 0$), respectively. $\phi(x, t)$ represents the transverse normal rotation about the y-axis, and t is time. The normal and transverse stresses can be represented as follows:

$$\sigma_x = Q_{11}(z)(\varepsilon_x(x) - \alpha(z)\Delta T(z)), \quad \tau_{xz} = Q_{55}(z)\gamma_{xz}(x), \quad (17)$$

where the elastic elements $Q_{11}(z)$ and $Q_{55}(z)$ are

$$Q_{11}(z) = \frac{E(z)}{(1 - v^2(z))}, \quad Q_{55}(z) = \frac{E(z)}{2(1 + v(z))} = G(z). \quad (18)$$

The governing equations of motion are derived from Hamilton's principle as follows:

$$\delta \int_0^t (T - \Pi + \gamma_{\mathrm{p}})\mathrm{d}t = 0, \quad (19)$$

where T, Π, and γ_{p} are the kinetic, potential (or elastic), and external potential energy, respectively. Finally, the differential equations of motion are obtained as follows:

$$\begin{cases} A_{11}\dfrac{\partial^2 u_0}{\partial x^2} + B_{11}\dfrac{\partial^2 \phi}{\partial x^2} + \dfrac{\partial N_x^{\mathrm{T}}}{\partial x} = I_1\dfrac{\partial^2 u_0}{\partial t^2} + I_2\dfrac{\partial^2 \phi}{\partial t^2}, \\[2mm] KA_{55}\left(\dfrac{\partial^2 w_0}{\partial x^2} + \dfrac{\partial \phi}{\partial x}\right) + N_{x_0}\dfrac{\partial^2 w_0}{\partial x^2} = I_1\dfrac{\partial^2 w_0}{\partial t^2}, \\[2mm] B_{11}\dfrac{\partial^2 u_0}{\partial x^2} + D_{11}\dfrac{\partial^2 \phi}{\partial x^2} - KA_{55}\left(\dfrac{\partial w_0}{\partial x} + \phi\right) + \dfrac{\partial M_x^{\mathrm{T}}}{\partial x} = I_2\dfrac{\partial^2 u_0}{\partial t^2} + I_3\dfrac{\partial^2 \phi}{\partial t^2}. \end{cases} \quad (20)$$

A_{11}, B_{11}, D_{11}, A_{55} and also the inertia terms I_1, I_2, I_3 are non-linear functions of x and are defined by

$$\begin{cases} (A_{11}, B_{11}, D_{11}) = \displaystyle\int_{-h/2}^{h/2} Q_{11}(z)(1, z, z^2)\mathrm{d}z, \\[3mm] A_{55} = \displaystyle\int_{-h/2}^{h/2} Q_{55}(z)\mathrm{d}z, \quad (I_1, I_2, I_3) = \displaystyle\int_{-h/2}^{h/2} \rho(z)(1, z, z^2)\mathrm{d}z. \end{cases} \quad (21)$$

In this study, the bottom surface temperature of the beam is ascribed to the reference temperature, i.e., $T_{\mathrm{Ref}} = T_{\mathrm{b}}$, and

$$T(z) = T(z) - T_{\mathrm{Ref}}. \tag{22}$$

The following nondimensional quantities make it possible that these studied results are independent of dimensions:

$$\begin{cases} \xi = \dfrac{x}{L}, \quad (u, w) = \left(\dfrac{u_0}{h}, \dfrac{w_0}{h}\right), \quad \eta = \dfrac{L}{h}, \quad \tau = \dfrac{t}{L}\sqrt{\dfrac{A_{110}}{I_{10}}}, \quad M_x^* = \dfrac{M_x^{\mathrm{T}}h}{D_{110}}, \\[3mm] (N_x^*, \lambda_{x_0}) = \left(\dfrac{N_x^{\mathrm{T}}}{A_{110}}, \dfrac{N_{x_0}}{A_{110}}\right), \quad \omega = \Omega L\sqrt{\dfrac{I_{10}}{A_{110}}}, \quad (\overline{I}_1, \overline{I}_2, \overline{I}_3) = \left(\dfrac{I_1}{I_{10}}, \dfrac{I_2}{I_{10}h}, \dfrac{I_3}{I_{10}h^2}\right), \\[3mm] (a_{11}, a_{55}, b_{11}, d_{11}) = \left(\dfrac{A_{11}}{A_{110}}, \dfrac{A_{55}}{A_{110}}, \dfrac{B_{11}}{A_{110}h}, \dfrac{D_{11}}{A_{110}h^2}\right), \\[3mm] (\overline{a}_{11}, \overline{a}_{55}, \overline{b}_{11}, \overline{d}_{11}) = \left(\dfrac{A_{11}h^2}{D_{110}}, \dfrac{A_{55}h^2}{D_{110}}, \dfrac{B_{11}h}{D_{110}}, \dfrac{D_{11}}{D_{110}}\right), \quad \gamma = \dfrac{A_{110}h_0^2}{D_{110}}. \end{cases} \tag{23}$$

In the above equations, N_{x_0} is the external axial load, A_{110}, D_{110}, and I_{10} are the same as A_{11}, D_{11}, and I_1 in the pure metal beam without porosity and nanofillers. According to Eq. (23), the governing equation (20) is rewritten in the nondimensional form as follows:

$$\begin{cases} a_{11}\dfrac{\partial^2 u}{\partial \xi^2} + b_{11}\dfrac{\partial^2 \phi}{\partial \xi^2} + \eta\dfrac{\partial N_x^*}{\partial \xi} = \overline{I}_1\dfrac{\partial^2 u}{\partial \tau^2} + \overline{I}_2\dfrac{\partial^2 \phi}{\partial \tau^2}, \\[3mm] Ka_{55}\left(\dfrac{\partial^2 w}{\partial \xi^2} + \eta\dfrac{\partial \phi}{\partial \xi}\right) + \lambda_{x_0}\dfrac{\partial^2 w}{\partial \xi^2} = \overline{I}_1\dfrac{\partial^2 w}{\partial \tau^2}, \\[3mm] \overline{b}_{11}\dfrac{\partial^2 u}{\partial \xi^2} + \overline{d}_{11}\dfrac{\partial^2 \phi}{\partial \xi^2} - K\overline{a}_{55}\eta\left(\dfrac{\partial w}{\partial \xi} + \eta\phi\right) + \eta\dfrac{\partial M_x^*}{\partial \xi} = \gamma\left(\overline{I}_2\dfrac{\partial^2 u}{\partial \tau^2} + \overline{I}_3\dfrac{\partial^2 \phi}{\partial \tau^2}\right). \end{cases} \tag{24}$$

In the same way, the boundary conditions can be nondimensional.

It is assumed that the sum of the static and dynamic displacement fields leads to the total displacement field, i.e.,

$$u = u_{\mathrm{S}} + u_{\mathrm{D}}, \quad w = w_{\mathrm{S}} + w_{\mathrm{D}}, \quad \phi = \phi_{\mathrm{S}} + \phi_{\mathrm{D}}, \tag{25}$$

where the subscripts 'S' and 'D' refer to the points in the static and dynamic fields, respectively. The primitive stress originating from the stable thermal field can be calculated by solving the static equations.

$$\begin{cases} a_{11}\dfrac{\partial^2 u_{\mathrm{S}}}{\partial \xi^2} + b_{11}\dfrac{\partial^2 \phi_{\mathrm{S}}}{\partial \xi^2} + \eta\dfrac{\partial N_x^*}{\partial \xi} = 0, \quad Ka_{55}\left(\dfrac{\partial^2 w_{\mathrm{S}}}{\partial \xi^2} + \eta\dfrac{\partial \phi}{\partial \xi}\right) = 0, \\[3mm] \overline{b}_{11}\dfrac{\partial^2 u_{\mathrm{S}}}{\partial \xi^2} + \overline{d}_{11}\dfrac{\partial^2 \phi_{\mathrm{S}}}{\partial \xi^2} - K\overline{a}_{55}\eta\left(\dfrac{\partial w_{\mathrm{S}}}{\partial \xi} + \eta\phi_{\mathrm{S}}\right) + \eta\dfrac{\partial M_x^*}{\partial \xi} = 0. \end{cases} \tag{26}$$

Obviously, Eq. (26) is obtained by dropping the inertia terms and λ_{x_0} in Eq. (24). According to Eqs. (24) and (25), the dynamic field equations will be as follows:

$$\begin{cases} a_{11}\dfrac{\partial^2 u_{\mathrm{D}}}{\partial \xi^2} + b_{11}\dfrac{\partial^2 \phi_{\mathrm{D}}}{\partial \xi^2} = \overline{I}_1\dfrac{\partial^2 u_{\mathrm{D}}}{\partial \tau^2} + \overline{I}_2\dfrac{\partial^2 \phi_{\mathrm{D}}}{\partial \tau^2}, \\[3mm] Ka_{55}\left(\dfrac{\partial^2 w_{\mathrm{D}}}{\partial \xi^2} + \eta\dfrac{\partial \phi_{\mathrm{D}}}{\partial \xi}\right) + \lambda_{x_0}\dfrac{\partial^2 w_{\mathrm{D}}}{\partial \xi^2} = \overline{I}_1\dfrac{\partial^2 w_{\mathrm{D}}}{\partial \tau^2}, \\[3mm] \overline{b}_{11}\dfrac{\partial^2 u_{\mathrm{D}}}{\partial \xi^2} + \overline{d}_{11}\dfrac{\partial^2 \phi_{\mathrm{D}}}{\partial \xi^2} - K\overline{a}_{55}\eta\left(\dfrac{\partial w_{\mathrm{D}}}{\partial \xi} + \eta\phi_{\mathrm{D}}\right) = \gamma\left(\overline{I}_2\dfrac{\partial^2 u_{\mathrm{D}}}{\partial \tau^2} + \overline{I}_3\dfrac{\partial^2 \phi_{\mathrm{D}}}{\partial \tau^2}\right). \end{cases} \tag{27}$$

The boundary conditions in the dynamic analysis become homogeneous.

3.2 Thermal field

The beam is affected by the thermal gradient across the thickness direction before undergoing dynamic deformation. It is considered that the upper and lower beam surfaces are held at the temperatures T_u and T_b, respectively. Thus, the thermal boundary conditions are

$$T = T_b \rightarrow z = -\frac{h}{2}, \quad T = T_u \rightarrow z = \frac{h}{2}. \tag{28}$$

We assume that the temperature changes linearly across the thickness direction, i.e.,

$$T(z) = T_b + \Delta T_{tot}\left(\frac{z}{h} + \frac{1}{2}\right), \tag{29}$$

where

$$\Delta T_{tot} = T_u - T_b. \tag{30}$$

3.3 GDQM

The GDQM, as a numerical solution method for initial and/or boundary problems, is implemented for solving the equations of motion. The GDQM has good accuracy and a fast convergence trend with the minimal computational effort vis-a-vis other numerical methods[31]. For more details about the GDQM, the readers may refer to Refs. [31] and [32]. For the sake of providing a very accurate generalized differential quadrature (GDQ) solution here, the Chebyshev-Gauss-Lobatto grid points are used[32], i.e.,

$$\xi_i = \frac{1}{2}\left(1 - \cos\left(\frac{i-1}{N-1}\pi\right)\right), \quad i = 1, 2, \cdots, N. \tag{31}$$

3.4 Thermal vibration analysis

What should be denoted is that applying the static displacement results in a dimensionless axial force λ_{x_0}.

$$\lambda_{x_0} = \frac{-N_x^T}{A_{110}} = -N_x^*. \tag{32}$$

With respect to Eq. (27), the following thermal vibration equations of the FG porous beam can be obtained:

$$\begin{cases} a_{11}\dfrac{\partial^2 u_D}{\partial \xi^2} + b_{11}\dfrac{\partial^2 \phi_D}{\partial \xi^2} = \overline{I}_1\dfrac{\partial^2 u_D}{\partial \tau^2} + \overline{I}_2\dfrac{\partial^2 \phi_D}{\partial \tau^2}, \\[3mm] Ka_{55}\left(\dfrac{\partial^2 w_D}{\partial \xi^2} + \eta\dfrac{\partial \phi_D}{\partial \xi}\right) - N_x^*\dfrac{\partial^2 w_D}{\partial \xi^2} = \overline{I}_1\dfrac{\partial^2 w_D}{\partial \tau^2}, \\[3mm] \overline{b}_{11}\dfrac{\partial^2 u_D}{\partial \xi^2} + \overline{d}_{11}\dfrac{\partial^2 \phi_D}{\partial \xi^2} - K\overline{a}_{55}\eta\left(\dfrac{\partial w_D}{\partial \xi} + \eta\phi_d\right) + \eta\dfrac{\partial M_x^*}{\partial \xi} = \gamma\left(\overline{I}_2\dfrac{\partial^2 u_D}{\partial \tau^2} + \overline{I}_3\dfrac{\partial^2 \phi_D}{\partial \tau^2}\right). \end{cases} \tag{33}$$

Since vibration is harmonic, the deflections can be stated as follows:

$$u(x,t) = w(x)e^{-i\omega t}, \quad w(x,t) = u(x)e^{-i\omega t}, \quad \phi(x,t) = \varphi(x)e^{-i\omega t}, \tag{34}$$

where $i = \sqrt{-1}$, and ω is the nondimensional fundamental frequency. Applying the GDQ to the equations of motion and the related boundary conditions leads to the following set of linear algebraic equations:

$$\begin{pmatrix} \boldsymbol{S}_{bb} & \boldsymbol{S}_{bd} \\ \boldsymbol{S}_{db} & \boldsymbol{S}_{dd} \end{pmatrix}\begin{pmatrix} \boldsymbol{U}_b \\ \boldsymbol{U}_d \end{pmatrix} - N_x^*\begin{pmatrix} \boldsymbol{0} & \boldsymbol{0} \\ \boldsymbol{A}_{db} & \boldsymbol{A}_{dd} \end{pmatrix}\begin{pmatrix} \boldsymbol{U}_b \\ \boldsymbol{U}_d \end{pmatrix} = \omega^2\begin{pmatrix} \boldsymbol{0} & \boldsymbol{0} \\ \boldsymbol{0} & \overline{\boldsymbol{I}}_i \end{pmatrix}\begin{pmatrix} \boldsymbol{U}_b \\ \boldsymbol{U}_d \end{pmatrix}, \tag{35}$$

where

$$U_{\mathrm{b}} = (u_{\mathrm{b}}, w_{\mathrm{b}}, \phi_{\mathrm{b}})^{\mathrm{T}}, \tag{36}$$

$$U_{\mathrm{d}} = (u_{\mathrm{d}}, w_{\mathrm{d}}, \phi_{\mathrm{d}})^{\mathrm{T}}. \tag{37}$$

In Eqs. (35)–(37), the subscripts 'b' and 'd' refer to the points on the boundary and in the interior domain, respectively, and $\overline{I}_i$ is the nondimensional inertia term matrix. Eliminating the boundary degrees of freedom provides the underlying equation as follows:

$$(S - \omega^2 I)u_{\mathrm{d}} = 0, \tag{38}$$

where

$$S = (S_{\mathrm{dd}} + A_{\mathrm{dd}}) - (S_{\mathrm{db}} + A_{\mathrm{db}})S_{\mathrm{bb}}^{-1}S_{\mathrm{bd}}. \tag{39}$$

Clearly, the square of the lowest positive eigenvalue of Eq. (39) gives the frequency of the considered beam. By solving the generalized eigenvalue problem of Eq. (39), the beam frequency can be obtained.

4 Numerical results and discussion

First, we consider the effects of GPLs, porosity, and temperature on the vibrations of the nanocomposite beams. The main parameters assessed in this paper are the distribution model, the weight fraction W_{GPL}, the geometry, the size of GPLs, the porosity coefficient, the porosity distribution, the boundary condition, and the thermal loading. Aluminum, copper, nickel, magnesium, and titanium metals play the role of material matrix in this study. According to Refs. [24] and [33]–[36], the properties of these materials are shown in Table 1. The material properties and geometric parameters of GPLs are as follows[10,37–38]:

$$\begin{cases} w_{\mathrm{GPL}} = 1.5\,\mu\mathrm{m}, \quad l_{\mathrm{GPL}} = 2.5\,\mu\mathrm{m}, \quad t_{\mathrm{GPL}} = 1.5\,\mathrm{nm}, \quad E_{\mathrm{GPL}} = 1.01\,\mathrm{TPa}, \\ \rho_{\mathrm{GPL}} = 1\,062.5\,\mathrm{kg}\cdot\mathrm{m}^{-3}, \quad \nu_{\mathrm{GPL}} = 0.186, \quad \alpha_{\mathrm{GPL}} = -3.75\times10^{-6}\,\mathrm{K}^{-1}. \end{cases}$$

Table 1 Typical material properties of metals

Material	Density/(kg·m^{-3})	Poisson's ratio	Young's modulus/GPa	Thermal expansion coefficient/K^{-1}
Aluminum	2 689.8	0.34	68.3	23×10^{-6}
Copper	8 960	0.34	130	17×10^{-6}
Nickel	8 908	0.31	210	13×10^{-6}
Magnesium	1 740	0.35	45	25×10^{-6}
Titanium	4 506	0.33	116	8.6×10^{-6}

4.1 Validation and convergence study

The free vibration and elastic buckling of FG porous nanocomposite beams have been investigated by Kitipornchai et al.[39]. The results obtained in this study for $\Delta T_{\mathrm{tot}} = 0$ are compared with those in Ref. [39].

Similar to the analysis of the free vibration, the critical buckling load is obtained through solving the concluded algebraic system. The nondimensional critical buckling load and natural frequency attained in the present analysis are compared with the similar ones given in Ref. [39] in Tables 2 and 3. The data show that our results are in good agreement with the previously reported ones. The differences are in the range from 0% to 0.36%.

Figure 3 shows the convergency of the results. As observed, the convergence rate of the GDQ is obviously high. At $N = 7$, the beam frequency converges to a certain desirable amount.

Table 2 Nondimensional buckling load of the porous copper-matrix beams reinforced by GPL model A with Distribution 1 under clamped-clamped conditions, where $l/h = 20$

$W_{\mathrm{GPL}}/\%$	n	$e_0 = 0.0$		$e_0 = 0.2$		$e_0 = 0.4$		$e_0 = 0.6$	
		Present study	Ref. [39]	Present study	Ref. [39]	Present study	Ref. [39]	Present study	Ref. [39]
1	2	0.008 526	0.008 550	0.007 215	0.007 218	0.005 924	0.005 917	0.004 650	0.004 647
	6	0.014 274	0.014 323	0.013 049	0.013 057	0.011 794	0.011 784	0.010 496	0.010 486
	10	0.014 746	0.014 798	0.013 567	0.013 572	0.012 347	0.012 333	0.011 067	0.011 063
	14	0.014 875	0.014 929	0.013 705	0.013 714	0.012 503	0.012 486	0.011 232	0.011 224
	18	0.014 931	0.014 982	0.013 760	0.013 773	0.012 568	0.012 549	0.011 296	0.011 290
	10 000	0.015 014	0.015 065	0.013 853	0.013 863	0.012 660	0.012 645	0.011 397	0.011 392
0	14	0.007 946	0.007 946	0.007 313	0.007 316	0.006 696	0.006 693	0.006 076	0.006 076
	10 000	0.007 983	0.007 986	0.007 359	0.007 362	0.006 742	0.006 745	0.006 132	0.006 135

Table 3 Nondimensional frequency of the porous copper-matrix beams reinforced by GPL model A with Distribution 1 under clamped-clamped conditions, where $l/h = 20$

| $W_{\mathrm{GPL}}/\%$	n	$e_0 = 0.0$		$e_0 = 0.2$		$e_0 = 0.4$		$e_0 = 0.6$	
		Present study	Ref. [39]	Present study	Ref. [39]	Present study	Ref. [39]	Present study	Ref. [39]
1	2	0.337 1	0.337 6	0.321 7	0.321 7	0.304 4	0.304 2	0.284 6	0.284 5
	6	0.438 1	0.439 0	0.433 4	0.433 6	0.429 1	0.428 9	0.426 1	0.425 9
	10	0.445 5	0.446 4	0.442 0	0.442 1	0.439 0	0.438 8	0.437 3	0.437 2
	14	0.447 5	0.448 4	0.444 2	0.444 4	0.441 8	0.441 5	0.440 5	0.440 3
	18	0.448 3	0.449 2	0.445 1	0.445 4	0.442 9	0.442 6	0.441 7	0.441 6
	10 000	0.449 6	0.450 5	0.446 6	0.446 8	0.444 5	0.444 2	0.443 7	0.443 6
0	14	0.315 9	0.315 9	0.313 4	0.313 4	0.312 2	0.312 1	0.312 8	0.312 8
	10 000	0.316 6	0.316 7	0.314 3	0.314 4	0.313 2	0.313 2	0.314 2	0.314 2
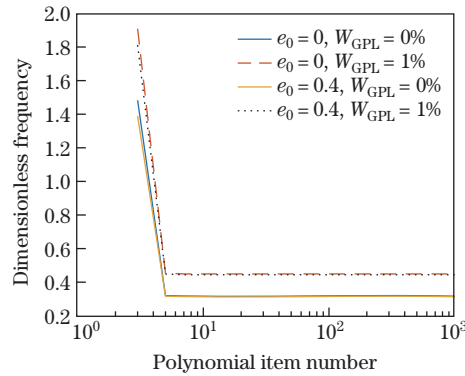
Fig. 3 Convergency of the nondimensional frequency of the nanocomposite copper-matrix beams reinforced by GPL model A with Distribution 1 under clamped-clamped conditions, where $l/h = 20$, and $\Delta T_{\mathrm{tot}} = 250\,\mathrm{K}$ (color online)

4.2 Analysis of the thermal vibration for $\Delta T_{\mathrm{tot}} = 250\,\mathrm{K}$

As mentioned before, we consider a multilayer beam because the multilayer structure makes the beam construction process easier. Two points are considered based on the multilayer structure of the beam. First, the results obtained from the vibration of the multilayer beam should be close to the results of the continuous one ($n = 1\,000$). Second, to save cost and time, the number of beam layers should be kept to be the minimum. To achieve these purposes, the thermal vibration of the beams with various numbers of layers is investigated (see Table 4). The results show that $n = 14$ meets the aforementioned points. Figure 4 displays the reinforced effects of GPLs on the thermal vibration frequency.

Table 4 Nondimensional frequency of the porous copper-matrix beams reinforced by GPL model A with Distribution 1 under clamped-clamped conditions, where $l/h = 20$, and $\Delta T_{\text{tot}} = 250\,\text{K}$

$W_{\text{GPL}}/\%$	n	$e_0 = 0.0$	$e_0 = 0.2$	$e_0 = 0.4$	$e_0 = 0.6$
	2	0.542 7	0.517 9	0.489 5	0.456 1
	6	0.377 9	0.376 8	0.376 3	0.377 3
1	10	0.411 0	0.409 7	0.408 9	0.409 4
	14	0.423 3	0.421 5	0.420 6	0.420 9
	20	0.440 7	0.439 6	0.439 8	0.440 0
	1 000	0.449 2	0.446 3	0.444 3	0.443 4
0	20	0.311 5	0.310 8	0.311 4	0.312 1
	1 000	0.316 3	0.314 0	0.312 9	0.313 9

Another investigated case is the comparison of the reinforced effects of GPLs on the beams with various metal matrices. As observed in Fig. 5, by adding GPLs to the beams, the frequency increases for all beams with various metal matrices. Regarding the rather high mass density of copper, it is predictable that the frequency increase in the copper beam is higher than the frequency increase in any of the other beams. The reason is that, under the same weight fraction, the added volume content of GPLs in the copper beam is larger, which means that more GPLs are used in this case. Although the mass density of nickel is as large as that of copper, its Young's modulus is much higher than that of copper, indicating that the enhancement of the effective Young's modulus of the nickel nanocomposite beam is relatively limited. As a consequence of the above-mentioned reasons, we concentrate on the copper matrix porous nanocomposites in the following discussion. Figure 5 shows the effects of different GPL models on the thermal vibration frequency of the porous beams with various porosity coefficients.
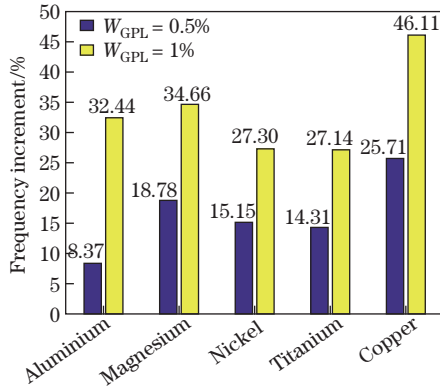
Fig. 4 Effects of GPLs on the thermal frequency variation of the porous beams reinforced by GPL model A with Distribution 1 versus different metal matrices under clamped-clamped conditions, where $e_0 = 0.5$, $l/h = 20$, and $\Delta T_{\text{tot}} = 250\,\text{K}$ (color online)
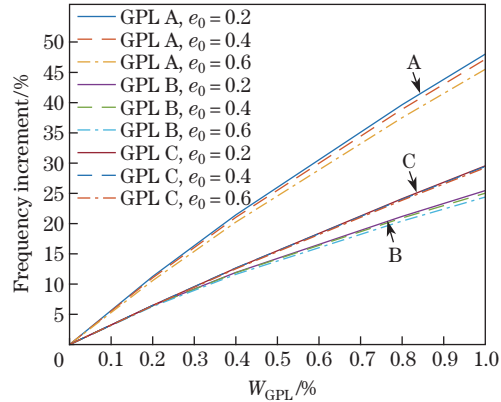
Fig. 5 Effects of the porosity coefficient and GPL models on the thermal frequency variations of the nanocomposite opper-matrix beams with Distribution 1 under clamped-clamped conditions, where $l/h = 20$, and $\Delta T_{\text{tot}} = 250\,\text{K}$ (color online)

For Distribution 1, in the three GPL models, introducing a small amount of GPLs significantly grows the frequency and stiffness of the beams. Besides, the GPL models have a great effect on the GPL reinforced property. GPL model A has the most reinforced effect on the porous beams, while GPL models C and B are in order of the second and the third, respectively. The last point is that the porosity coefficient does not have a sensible effect on the thermal vibration frequency change. As the porosity coefficient climbs, the stiffness decreases

negligibly. The beam reinforced by GPL model C is approximately independent of the porosity coefficient. Therefore, in this certain model, the plots with various porosity coefficients coincide with each other. Figure 6 shows the effects of the GPL models as well as the porosity distributions on the thermal vibration frequency of the nanocomposite beam. In Fig. 6 and the following figures, Dis. is the abbreviation of Distribution.

The beam reinforced by GPL model A with Distribution 1 has the maximum frequency, which means that at the same weight fraction, most effective stiffness belongs to the beam that has either Distribution 1 or GPL model A. The effects of the porosity distribution on the frequency variations in the beams reinforced by various GPL models are shown in Fig. 7. It can be seen that the frequency increment is affected by the porosity distributions in GPL models A and B, whereas is independent of the porosity distribution in GPL model C. By comparing Figs. 5, 6, and 7, it can be deduced that both the GPL models and the porosity distributions are effective in the frequency increment, but the effects of the former are much greater than the effects of the latter. Figure 8 indicates the effects of the geometry and size of GPLs on the thermal vibration frequency of the porous nanocomposite beams.
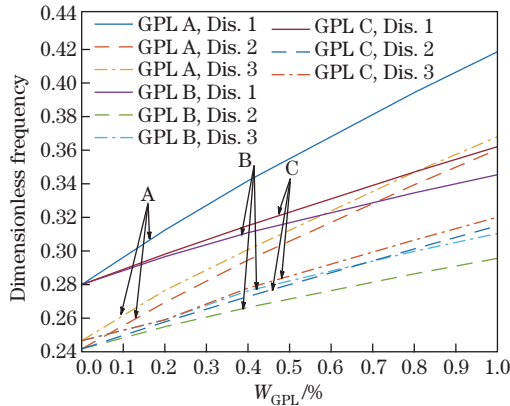
Fig. 6 Effects of the GPL models and the porosity distributions on the thermal frequency of the copper-matrix beams under clamped-clamped conditions, where $e_0 = 0.5$, $l/h = 20$, and $\Delta T_{\mathrm{tot}} = 250\,\mathrm{K}$ (color online)
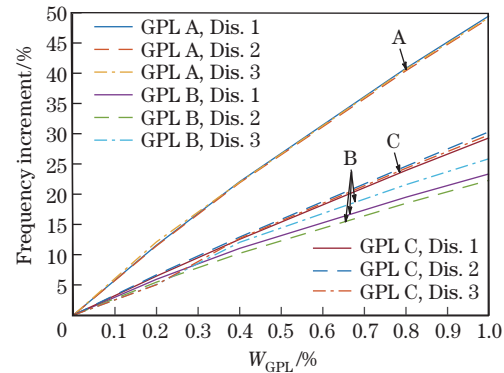
Fig. 7 Effects of the GPL models and the porosity distributions on the thermal frequency variations of the copper-matrix beams under clamped-clamped conditions, where $e_0 = 0.5$, $l/h = 20$, and $\Delta T_{\mathrm{tot}} = 250\,\mathrm{K}$ (color online)

As observed in Fig. 8, the effects of $l_{\mathrm{GPL}}/t_{\mathrm{GPL}}$ and $l_{\mathrm{GPL}}/w_{\mathrm{GPL}}$ (assuming constant l_{GPL}) on the thermal vibration frequency are investigated. The thermal frequency is shown against $l_{\mathrm{GPL}}/t_{\mathrm{GPL}}$. As $l_{\mathrm{GPL}}/t_{\mathrm{GPL}}$ rises, the frequency enhances. For a certain $l_{\mathrm{GPL}}/t_{\mathrm{GPL}}$, by growing $l_{\mathrm{GPL}}/w_{\mathrm{GPL}}$, the frequency decreases because the surface area of the platelets diminishes. As noticed around $l_{\mathrm{GPL}}/t_{\mathrm{GPL}} > 100$, there is an inflection point showing the decrease in the rate of increasing the thermal frequency. This is because the distribution of the graphene in the composite may be poor. When $l_{\mathrm{GPL}}/t_{\mathrm{GPL}} > 10^4$, the frequency orients to a certain amount, and is independent of $l_{\mathrm{GPL}}/w_{\mathrm{GPL}}$. In other words, the thermal frequency is independent of the size of graphene due to the poor dispersion of graphene for $l_{\mathrm{GPL}}/t_{\mathrm{GPL}} > 10^4$. A similar trend of Fig. 8 is obtained for free vibration and critical buckling load in Ref. [37]. The effects of boundary conditions on the frequency change of the porous beams reinforced by various GPL models are depicted in Fig. 9, where C represents clamped, F represents free, and H represents hinged.
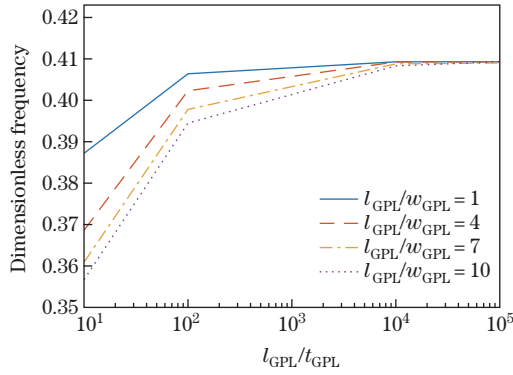
Fig. 8 Effects of the size and geometry of GPLs on the dimensionless frequency of the nanocomposite copper-matrix beams reinforced by GPL model A with Distribution 1 under clamped-clamped conditions, where $e_0 = 0.5$, $l/h = 20$, $W_{GPL} = 1\%$, and $\Delta T_{tot} = 250$ K) (color online)
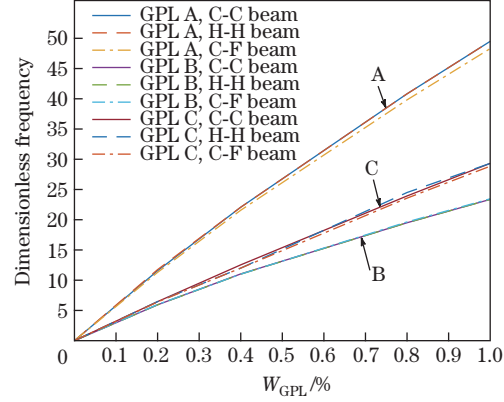
Fig. 9 Effects of boundary conditions on the thermal frequency increment of the copper-matrix beams with Distribution 1, where $e_0 = 0.5$, $l/h = 20$, and $\Delta T_{tot} = 250$ K (color online)

Distribution 1 is taken for all of the beams. As pointed out, introducing GPLs leads to the frequency increase for all boundary conditions. Also, it is evident that the boundary conditions have few effects on the frequency increment for all types of GPL models. The effects of the boundary conditions on the frequency increment in beams reinforced by GPL model A are more remarkable than the other beams. The nondimensional frequency amounts of the porous nanocomposite beam reinforced by GPLs are listed for different slenderness ratios in Table 5. Clearly, the frequency decreases with increasing the slenderness ratio.

Table 5 Nondimensional frequency in the copper-matrix beams reinforced by GPL model A with Distribution 1 and various slenderness ratios under clamped-clamped conditions, where $e_0 = 0.5$, and $\Delta T_{tot} = 250$ K

L/h	$W_{GPL}/\%$					
	0.0	0.2	0.4	0.6	0.8	1.0
20	0.280 0	0.312 4	0.341 8	0.363 5	0.394 3	0.418 6
30	0.143 2	0.176 4	0.194 1	0.210 6	0.225 5	0.240 6
40	0.072 3	0.089 4	0.105 6	0.120 2	0.133 6	0.146 4

4.3 Effects of the thermal gradient (ΔT_{tot}) on the vibration

In the beams reinforced by different GPL models and with various porosity distributions, the dimensionless frequency versus the thermal gradient is depicted in Fig. 10. It is shown that the frequency drops with the surge of the thermal gradient.

Figures 11, 12, and 13 represent the effects of ΔT_{tot} on the frequency of the beams reinforced by various GPL models and with different porosity coefficients. In all beams reinforced by various GPL models, the frequency and the porosity coefficient have an inverse relation if $\Delta T_{tot} = 0$. The boosting porosity coefficient results in the enhancement of the frequency for each certain non-zero ΔT_{tot}. For zero thermal gradient, the differences among the frequencies of the beams of various porosity coefficients are small. However, when ΔT_{tot} increases, the differences steadily increase. These findings clarify the fact that porous materials are appropriate candidates for structures used in cases of high thermal gradients. The frequency variations of the nanocomposite beams for various thermal gradients are shown in Fig. 14.
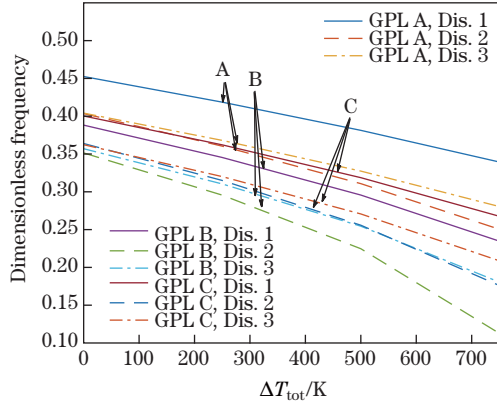
Fig. 10 Nondimensional frequency variations of the copper-matrix beams reinforced by different GPL models with different distributions under clamped-clamped conditions, where $e_0 = 0.5$, and $l/h = 20$ (color online)
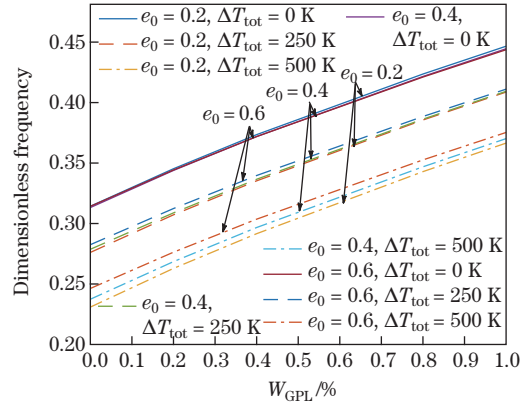

Fig. 11 Nondimensional frequency variations of the copper-matrix beams reinforced by GPL model A with Distribution 2 under clamped-clamped conditions, where $l/h = 20$ (color online)
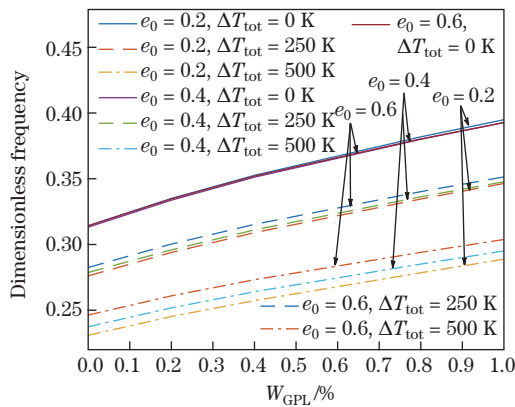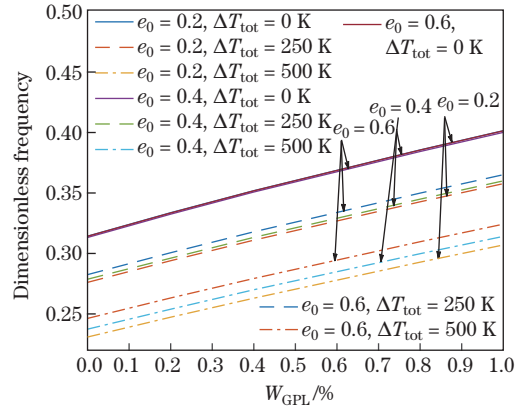

Fig. 12 Nondimensional frequency variations of the copper-matrix beams reinforced by GPL model B with Distribution 2 under clamped-clamped conditions, where $l/h = 20$) (color online)

Fig. 13 Nondimensional frequency variations of the copper-matrix beams reinforced by GPL model C with Distribution 1 under clamped-clamped conditions, where $l/h = 20$ (color online)

The frequency increment rises with the increase in the thermal gradient for a certain GPL weight fraction except the beam reinforced by GPL model B. This trend for GPL model A is more obvious than that for GPL model C. The frequency variations of the beams of various porosity coefficients reinforced by the GPL weight fraction are illustrated in Fig. 15.

The results show that the slope of the frequency curve increases when the thermal gradient for a pair of specified values of the porosity coefficient and the weight fraction increases. Increasing the thermal gradient leads to an inverse relation of the porosity coefficient and the frequency increment. For a specified GPL weight fraction, the frequency increment is the biggest for a beam with the minimum porosity coefficient. Figures 16, 17, and 18 display the effects of the porosity distribution on the frequency increment for various thermal gradients. In
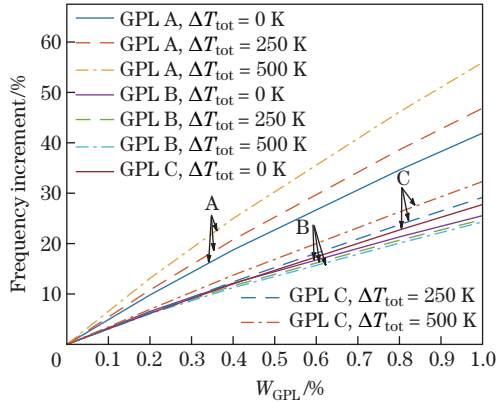
Fig. 14 Nondimensional frequency variations of the copper-matrix beams reinforced by different GPL models with Distribution 1 under clamped-clamped conditions, where $e_0 = 0.5$, and $l/h = 20$ (color online)
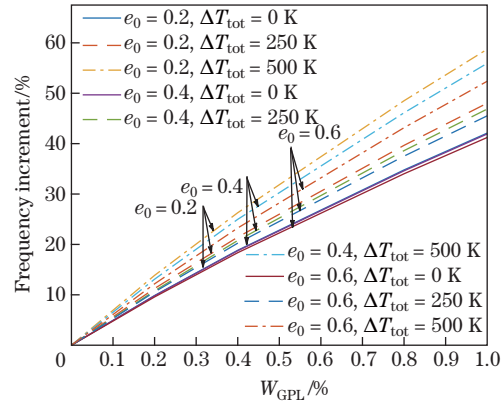

Fig. 15 Nondimensional frequency variations of the copper-matrix beams reinforced by GPL model A with Distribution 1 under clamped-clamped conditions, where $l/h = 20$ (color online)
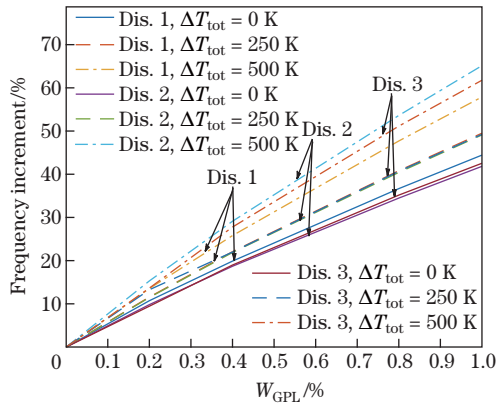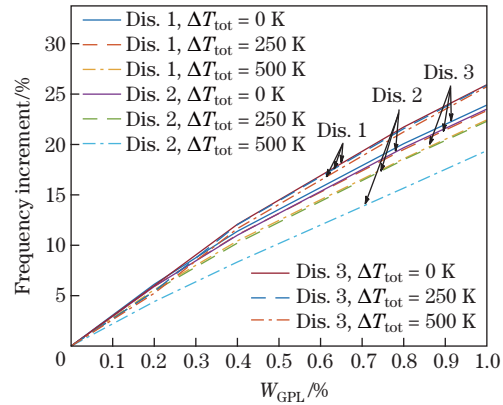

Fig. 16 Nondimensional frequency variations of the copper-matrix beams reinforced by GPL model A under clamped-clamped conditions, where $e_0 = 0.5$, and $l/h = 20$ (color online)

Fig. 17 Nondimensional frequency variations of the copper-matrix beams reinforced by GPL model B under clamped-clamped conditions, where $e_0 = 0.5$, and $l/h = 20$ (color online)

the beams reinforced by GPL models A and C, the frequency increment enhances when the thermal gradient for all porosity distributions increases. Moreover, when the thermal gradient increases, the frequency variations of the beams with Distribution 2 are greater than those with any other porosity distribution. As observed in Fig. 17, the frequency increment descends gradually in the nanocomposite beams reinforced by GPL model B by growing the thermal gradient. In Distribution 2, this descending rate is higher than any other porosity distribution.

Figure 19 shows the variations of the nondimensional frequency versus the GPL weight fraction for different ΔT_{tot} and boundary conditions, where C represents clamped, F represents free, and H represents hinged. According to Fig. 19, the frequency increment goes up due to the increase in the thermal gradient for all types of boundary conditions. But this increasing value is not the same. The maximum enhancement and the minimum enhancement of the frequency increment belong to the clamped-clamped and clamped-free beams, respectively.
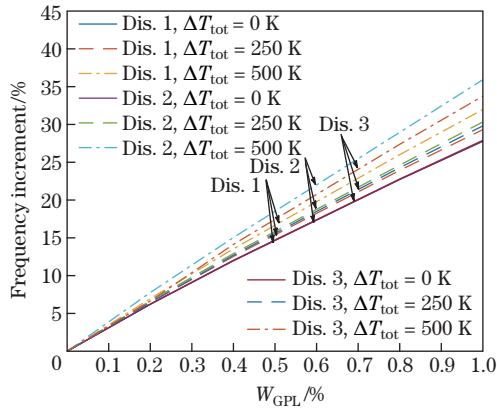
Fig. 18 Nondimensional frequency variations of the copper-matrix beams reinforced by GPL model C under clamped-clamped conditions, where $e_0 = 0.5$, and $l/h = 20$ (color online)
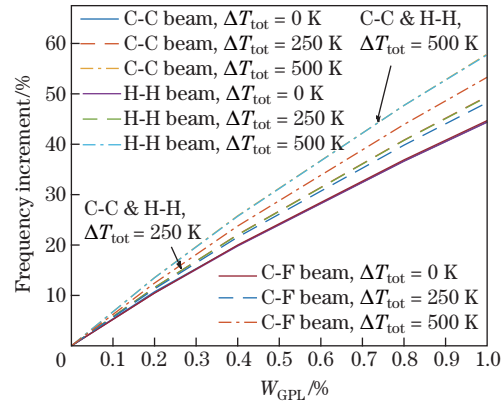
Fig. 19 Nondimensional frequency variations of the copper-matrix beam reinforced by GPL model A with Distribution 1 versus the GPL weight fraction under different boundary conditions, where $e_0 = 0.5$, and $l/h = 20$ (color online)

5 Conclusions

In this work, the thermal vibration of FG porous nanocomposite beams reinforced by GPLs is presented by using the Timoshenko beam theory. This study concentrates on the effects of porosity distributions and GPLs on the thermal vibration. The numerical results suggest that introducing a small amount of GPLs significantly improves the stiffness of the present structure. According to the mixture rule, the proposed beam behaves acceptably in high thermal gradients because of the negative thermal expansion coefficient of the nanofillers. Both the porosity distributions and the GPL models obviously affect the frequency increment, and the effects of the GPL models are greater. The effects of boundary conditions on the frequency increment are slightly negligible. According to the results, there is an inverse relation between the slenderness ratio and the frequency. The analysis of the effects of ΔT_{tot} on the beam frequency suggests that the beam frequency diminishes by growing the thermal gradient. Besides, it is concluded that the higher the porosity coefficient is, the greater the frequency for the non-zero thermal gradient is. Meanwhile, the effect of ΔT_{tot} on the frequency increment is different for those beams reinforced by GPL models and with various porosity distributions. Owing to the lightweight and high-strength properties, as well as the desirable behavior at high thermal gradients, these beams are recommended in new constructions.

References

[1] DELERUE, J. F., LOMOV, S. V., PAMAS, R. S., VERPOEST, I., and WEVERS, M. Pore network modeling of permeability for textile reinforcements. *Polymer Composites*, **24**, 344–357 (2003)

[2] BETTS, C. Benefits of metal foams and developments in modelling techniques to assess their

materials behaviour: a review. *Materials Science and Technology*, **28**, 129–143 (2012)

[3] CHOHRA, M., ADVANI, S. G., GOKEE, A., and YARLAGADDA, S. Modeling of filtration through multiple layers of dual scale fibrous porous media. *Polymer Composites*, **27**, 570–581 (2006)

[4] MAGNUCKI, K. and STASIEWICZ, P. Elastic buckling of a porous beam. *Journal of Theoretical and Applied Mechanics*, **42**, 859–868 (2004)

[5] GRYGOROWICZ, M., MAGNUCKI, K., and MALINOWSKI, M. Elastic buckling of a sandwich beam with variable mechanical properties of the core. *Thin-Walled Structures*, **87**, 127–132 (2015)

[6] CHEN, D., YANG, J., and KITIPORNCHAI, S. Elastic buckling and static bending of shear deformable functionally graded porous beam. *Composite Structures*, **133**, 54–61 (2015)

[7] CHEN, D., YANG, J., and KITIPORNCHAI, S. Free and forced vibrations of shear deformable functionally graded porous beams. *International Journal of Mechanical Science*, **108-109**, 14–22 (2016)

[8] EBRAHIMI, F., GHASEMI, F., and SALARI, E. Investigating thermal effects on vibration behavior of temperature-dependent compositionally graded Euler beams with porosities. *Meccanica*, **51**, 223–249 (2016)

[9] IIJIMA, S. Helical microtubules of graphitic carbon. *nature*, **354**, 56–58 (1991)

[10] RAFIEE, M. A., RAFIEE, J., WANG, Z., SONG, H., YU, Z. Z., and KORAKAR, N. Enhanced mechanical properties of nanocomposites at low graphene content. *ACS Nano*, **3**, 3884–3890 (2009)

[11] GONG, L., YOUNG, R. J., KINLOCH, I. A., RIAZ, I., JALIL, R., and NOVOSELOV, K. S. Optimizing the reinforcement of polymer-based nanocomposites by graphene. *ACS Nano*, **6**, 2086–2095 (2012)

[12] WU, H. L., YANG, J., and KITIPORNCHAI, S. Nonlinear vibration of functionally graded carbon nanotube-reinforced composite beams with geometric imperfections. *Composite Part B: Engineering*, **90**, 86–96 (2016)

[13] WATTANASAKULPONG, N. and UNGBHAKORN, V. Analytical solutions for bending, buckling and vibration responses of carbon nanotube-reinforced composite beams resting on elastic foundation. *Computational Materials Science*, **71**, 201–208 (2013)

[14] MOHAMMADI, S. and YAS, M. H. Modeling of elastic behavior of carbon nanotube reinforced polymer by accounting the interfacial debonding. *Journal of Reinforced Plastics and Composites*, **35**, 1477–1489 (2016)

[15] YAS, M. H., MOHAMMADI, S., ASTINCHAP, B., and HESHMATI, M. A comprehensive study on the thermo mechanical properties of multi-walled carbon nanotube/epoxy. *Journal of Composite Materials*, **50**, 2025–2034 (2015)

[16] YAS, M. H. and SAMADI, N. Free vibrations and buckling analysis of carbon nanotube-reinforced composite Timoshenko beams on elastic foundation. *International Journal of Pressure Vessel and Piping*, **98**, 119–128 (2012)

[17] LAI, R. and DANGI, C. Thermal vibrations of temperature-dependent functionally graded non-uniform Timoshenko nanobeam using nonlocal elasticity theory. *Materials Research Express*, **6**, 1–15 (2019)

[18] AREFI, M., MOHAMMAD-REZAEI, B. E., DIMITR, R., and TORNABENE, F. Free vibrations of functionally graded polymer composite nanoplates reinforced with graphene nanoplatelets. *Aerospace Science Technology*, **81**, 108–117 (2018)

[19] SHAHRJERDI, A. and YAVAR, I. S. Free vibration analysis of functionally graded graphene-reinforced nanocomposite beams with temperature-dependent properties. *Journal of the Brazilian Society of Mechanical Sciences and Engineering*, **40**, 25 (2018)

[20] SONG, M., KITIPORNCHAI, S., and YANG, J. Free and forced vibrations of functionally graded polymer composite plates reinforced with graphene nanoplatelets. *Composite Structures*, **159**, 579–588 (2017)

[21] ZAMAN, I., KNAN, H. C., DAI, J., KAWASHIMA, N., MICHELMORE, A., SOVI, A., DONG, S., LUONG, L., and MA, J. From carbon nanotubes and silicate layers to graphene platelets for polymer nanocomposites. *Nanoscale*, **4**, 4578–4586 (2012)

[22] LI, Z. L., YOUNG, R. J., WILSON, N. R., KINLOCH, I. A., VALLES, C., and LI, Z. Effect of the orientation of graphene-based nanoplatelets upon the Young's modulus of nanocomposites. *Composite Science and Technology*, **123**, 125–133 (2016)

[23] ZHENG, H. and JAGANANDHAM, K. Thermal conductivity and interface thermal conductance in composites of titanium with graphene platelets. *Journal of Heat Transfer*, **136**, 061301 (2014)

[24] BAKSHI, S., AKSHI, S., LAHIRI, D., and AGARWAL, A. Carbon nanotube reinforced metal matrix composites — a review. *International Materials Reviews*, **55**, 41–64 (2010)

[25] LAKES, R. Cellular solid structures with unbounded thermal expansion. *Journal of Materials Science Letters*, **15**, 475–477 (1996)

[26] ROBERTS, A. P. and GARBOCZI, E. J. Elastic moduli of model random three-dimensional closed-cell cellular solids. *Acta Materials*, **49**, 189–197 (2001)

[27] ROBERTS, A. P. and GARBOCZI, E. J. Computation of the linear elastic properties of random porous materials with a wide variety of microstructure. *Proceeding of Royal Society London, Ser. A*, **458**, 1033–1054 (2002)

[28] SHOKRIEH, M. M., ESMKHANI, M., SHOKRIEH, Z., and ZHAO, Z. Stiffness prediction of graphene nanoplatelet/epoxy nanocomposites by a combined molecular dynamics-micromechanics method. *Computional Materials Science*, **92**, 444–450 (2014)

[29] AFFDL, J. H. and KARDOS, J. L. The Halpin-Tsai equations: a review. *Polymer Engineering and Science*, **16**, 344–352 (1976)

[30] DE VILLORIA, R. G. and MIRAVETE, A. Mechanical model to evaluate the effect of the dispersion in nanocomposites. *Acta Materialia*, **55**, 3025–3031 (2007)

[31] SHU, C. *Differential Quadrature and Its Application in Engineering*, Springer-Verlag, London (2000)

[32] SHU, C. and DU, H. Implementation of clamped and simply supported boundary conditions in the GDQ free vibration analysis of beams and plates. *International Journal of Solid Structures*, **34**, 819–835 (1997)

[33] JAGANNADHAM, K. Thermal conductivity of copper-graphene composite films synthesized by electrochemical deposition with exfoliated graphene platelets. *Metallurgical and Materials Transactions B*, **43**, 316–324 (2012)

[34] HACKER, M., BURGHARDT, D., FLETCHER, L., GORDON, A., and PERUZZI, W. *Engineering and Technology*, the National Academies Press, New York, 50–75 (2015)

[35] TJONG, S. C. Recent progress in the development and properties of novel metal matrix nanocomposites reinforced with carbon nanotubes and graphene nanosheets. *Materials Science Engneering*, **74**, 281–350 (2013)

[36] LÜTJERING, G. and WILLIAMS, J. C. *Titanium*, Springer Science+Business Media, Berlin (2007)

[37] SHAINA, P. R., GEORGE, L., YADAV, V., and JAISWAL, M. Estimating the thermal expansion coefficient of graphene: the role of graphene-substrate interactions. *Journal of Physics*: *Condensed Matter*, **28**, 085301 (2016)

[38] LIU, F., MING, P., and LI, J. Ab initio calculation of ideal strength and phonon instability of graphene under tension. *Physical Review B*, **76**, 064120 (2007)

[39] KITIPORNCHAI, S., CHEN, D., and YANG, J. Free vibration and elastic buckling of functionally graded porous beams reinforced by graphene platelets. *Materials and Design*, **116**, 656–665 (2017)